Article

Added Value of Aerosol Observations of the Future AOS High Spectral Resolution Lidar with Respect to a Classic Backscatter Spaceborne Lidar Measurements

Flavien Cornut [1*], Laaziz El Amraoui [1], Juan Cuesta [2] and Jérôme Blanc [3]

[1*] flavien.cornut@meteo.fr ; Université de Toulouse, Météo-France, CNES, 42 av. Gaspard Coriolis, 31057 Toulouse Cedex 1, France
[2] cuesta@lisa.ipsl.fr ; Univ Paris Est Creteil and Université de Paris, CNRS, LISA, F-94010 Créteil, France
[2] Jerome.Blanc@cnes.fr ; CNES, 18 av. Edouard Belin, 31401 Toulouse Cedex 9, France

Abstract: In the context of the Atmospheric Observing System (AOS) international program, a new generation spaceborne lidar is expected to be in polar orbit for deriving new observations of aerosol and clouds. In this work, we analyze the added values of these new observations for characterizing aerosol vertical distribution. For this, synthetic observations are simulated using the BLISS lidar simulator in terms of backscatter coefficient at 532 nm. We consider two types of lidar instruments, an elastic backscatter lidar instrument and a high spectral resolution lidar (HSRL). These simulations are performed with atmospheric profiles from a Nature Run (NR) modeled by the MOCAGE Chemical Transport Model. In three case studies involving large events of different aerosol species, the added value of the HSRL channel for measuring aerosol backscatter profiles with respect to simple backscatter measurements is shown. Observations independent from an a-priori lidar Ratio assumption, as done typically for simple backscattering instruments, allows probing the vertical structure of aerosol layers without divergence, even in case of intense episodes. Relative error in the backscatter coefficient profiles are observed to lay between +40% and -40% for low abudancies, with mean biases between +5% and -5%. A 5-day study in the case of desert dust completes the study of the added value of the HSRL channel with relative mean bias from the NR of the order of 1.5%.

Keywords: Atmospheric-Observing-System; Aerosol; High-Spectral-Resolution-lidar

1. Introduction

The study and monitoring of atmospheric aerosols is a major issue for public health [1], environment [2], and climate [3]. However, one of the major remaining challenges is the good knowledge of their vertical distribution, necessary to document the direct and indirect effects on the climate [4]. Distinguishing a layer of particles above clouds allows the quantification of the cloud albedo impact on the atmospheric warming capacity of the aerosol. This phenomenon can lead to an early evaporation of clouds, which is considered as the typical semi-direct impact of particles on the climate, and a source of large uncertainties on weather prediction [5]. Moreover, it has been shown that aerosol radiative feedback induces maximum warming at low, medium or high altitudes, depending on whether the vertical structure of the aerosols is well mixed, with concentration increasing or decrasing with altitude, respectively. This phenomenon has an important impact on the stability of the aerosol-Planetary Boundary Layer (PBL) [6].

Advances on the understanding of the aerosols vertical distribution have been made possible thanks to the CALIOP (Cloud-Aerosol lidar with Orthogonal Polarization) spaceborne lidar onboard the CALIPSO (Cloud-Aerosol lidar and Infrared Pathfinder Satellite Observation) platform since 2006 [7–9]. The CALIOP instrument consists of elastic backscatter channels at two wavelengths λ (1064 nm, 532 nm) lidar with depolarization channel which allows the observation of the vertical distribution of aerosols. This enables the creation of global and inter-annual climatologies of aerosols vertical distribution, such as for desert dust (DD) [10]. The unprecedented amount of lidar data on the vertical aerosol characterization at global scale also allowed the development of Data Assimilation Systems (DAS) for several Chemical Transport Models (CTM) such as MOCAGE (*Modèle de Chimie Atmosphérique à Grande Échelle*) or the ECMWF/IFS (*European Center for Medium-Range Weather Forecast / Integrated Forecast System*). However, the inversion methods of elastic backscatter lidars such as CALIOP for deriving aerosol backscatter profiles are based on classic algorithms (such as the work from [11] and [12]) which rely on assumptions about the optical properties of the atmospheric aerosols. The main assumptions are an a-priori lidar Ratio (LR), ratio of the particular extinction and backscatter coefficients, which is intrinsic to each aerosol species/composition, and an aerosol free altitude for signal calibration (or normalization). This assumption may introduce large uncertainties, especially when the composition of the atmosphere varies along the vertical, whether it is composed of several layers with more or less homogeneous mixtures. All these factors could lead to unavoidable divergences in the inversion analysis, which limits the access to a well detailed restitution of the atmospheric column.

Many satellite lidar projects with various technologies succeed CALIOP. The ADM-Aeolus/ALADIN (Atmospheric Dynamics Mission/Atmospheric LAser Doppler INStrument) is the first space Doppler lidar [13], designed to monitor the wind velocity with a 355 nm laser inclined at 35 ° from the nadir, which also offer High Spectral Resolution lidar (HSRL) observations. The spectral-resolved system with a Fizeau spectrometer combined with a Fabry-Perot interferometer allowed to develop an aerosol L2A (Level 2 Aerosol) product to derive backscatter to extinction or scattering ratios as well as the aerosol optical thickness [14]. The future EarthCARE (Earth Cloud, Aerosol and Radiation Explorer) developed by the European Space Agency is an aerosols and clouds lidar with HSRL capability at high vertical resolution at 355 nm in orbit together with a Doppler radar [15]. The HSRL is a major innovation for retrieving the optical properties of particles [16]. It consists of separating the particular and the molecular backscattered signal thanks to an appropriate filter centered on the Mie scattering spectrum that occurs with Doppler shift phenomena. It allows the monitoring of the atmospheric geophysical parameters without any a-priori information on the chemical composition or the vertical distribution and the aerosol optical properties.

The AOS (Atmospheric Observing System) mission is an international program with a contribution from several spaces agencies [NASA (National Aeronautics Space Administration), CNES (Centre National d'Etudes Spatiales), Canadian Space Agency, Japan Aerospace Exploration Agency], part of the NASA's Earth Observing System program (EOS) (previously named Aerosol, Clouds, Convection and Precipitation (ACCP)). The program is dedicated to the observation of aerosols, clouds and precipitations, with a constellation of three satellites including a large set of complementary instruments [17]. An artist's view of the constellation is presented in Figure 10 in the appendix. The AOS-P1 platform aims to carry the very first HSRL lidar at 532 nm dedicated to the monitoring of both aerosols and clouds. In the same way as for EarthCare, the visible HSRL channel is expected to give more efficient retrieval, avoiding various sources of divergence specific to classic elastic backscatter lidar inversion methods. It is also more adapted to give better specification of aerosols, especially on the vertical, as well as new differentiable species, such as ice particles, polluted marine or smoke with different aging properties (smoke and fresh smoke) [18].

The objective of this study is to evaluate the added value of an AOS-type observation (AOS_HSRL) compared to an Elastic Backscatter-type observation (AOS_Backscatter), for a spaceborne lidar operating at 532 nm. This study is done within the framework of the AOS

doi:10.20944/preprints202212.0237.v1

mission, using the tools and instrumental parameters developed and determined for this purpose. In the first section of the current study, the method and the Synthetic Observations (SO) setup is described. It includes the simulation of a realistic atmosphere with the CTM MOCAGE that plays the role of Nature Run (NR) from which inputs are extracted for the observation simulator. Main lidar equations and a brief presentation of the lidar signal simulator software are also included. For the second section, we focus on the quantification of the added value f the HSRL technology for three events: (1) a Saharan dust event over the Mediterranean Sea that occurred in March 2018 and reached Greece, (2) a biomass burning episode due to intense wildfire in August 2018 in over Southern Canada and (3) an anthropogenic pollution event in the Beijing-Tianjin-Hebei region of China on February 2018. SO are performed and compared in terms of particular backscatter coefficient to focus on the capability to retrieve the vertical structures of aerosols. The comparison of the two sets of simulations with each other and with the NR allows to evaluate the added value of the HSRL technology in the context of a spaceborne lidar for the study of aerosols vertical distribution. Section 3 consider a larger period focused on the desert dust event (5 days) to perform a statistic comparison of aerosol different retrievals.

2. Retrieval of aerosol lidar synthetic observations

2.1. Method

The first step of this experiment consist of modeling and validating the NR. This atmosphere is expected to be sufficiently realistic for describing the events selected for this study in terms of aerosol abundance and chemical composition, and the respective aerosol optical properties (backscattering and extinction). In particular, the NR must have a good correspondence in terms of LR with the represented species to justify the hypotheses during the simulation of the AOS_Backscatter instrument.

The particle extinction and backscatter profiles are then extracted following a typical trajectory of a spaceborne lidar (we use CALIOP trajectories). These extracted aerosol profiles, meteorological fields and surface properties are integrated as input into an observation simulator for performing the simulations. In this study, the Backscatter lidar Signal Simulator (BLISS) software developed by the CNES is used. Note than this software is developed in the framework of the AOS mission in order to build the SO of several configurations. The simulator and the simulation setup will be presented later in the dedicated article.

For each event, two sets of simulations are performed: one with the standard Klett inversion method with AOS architecture (altitude, emitted power etc...) called AOS_Backscatter and a second one with the HSRL method called AOS_HSRL. The SO are then compared to each other and to the NR to access the added value of the HSRL channel for a spaceborne lidar. In the first time, the evaluations are made for each event on a single transect in order to visualize the temporal evolution of the observations along the trajectory. In a second step, a statistical analysis over 5 days from March, 20, 2018 to March, 25, 2018 ($\sim$ 20 orbits, $\sim$ 1700 profiles at 0.5 $^\circ \times$ 0.5 $^\circ$ resolution) is then performed for the specific case of the desert event. The experiment is schematized in Figure 1.

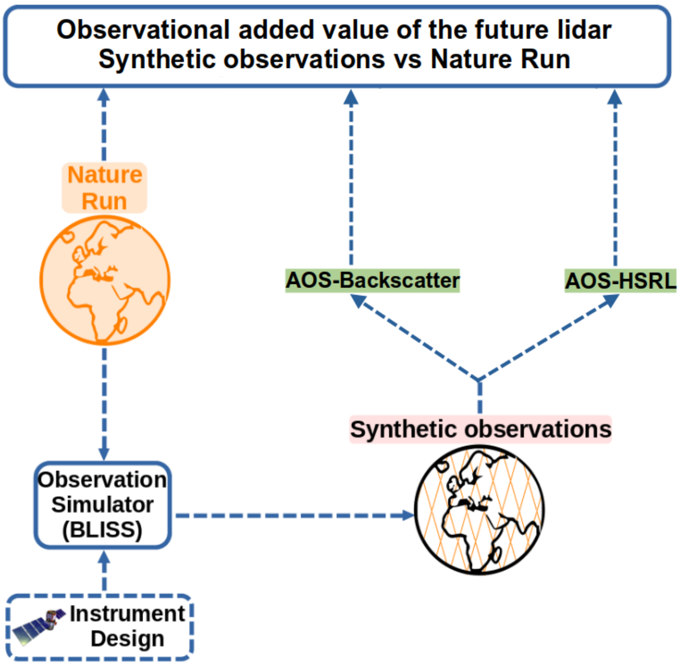

Figure 1. Schematic representation of the experience principle

2.2. The Nature Run 133

The NR is constructed by assimilating the MODIS (Moderate Resolution Imaging Spectroradiometer, [19]) Aerosol Optical Depth (AOD) data at 550 nm with a variational method in the MOCAGE CTM [20]. The period of simulation extends from January to September 2018 where the month of January is considered as the spin-up. Meteorological forecast is performed with ARPEGE (*Action de Recherche Petite Echelle Grande Echelle*) at 6 hour temporal resolution [21]. 134 135 136 137 138 139

2.2.1. The MOCAGE chemistry transport model 140

MOCAGE is an off-line 3D CTM developed by Météo-France that provides the chemical state of the atmosphere at a time $t + \Delta t$ based on its initial state (atmospheric composition at the time t), meteorological inputs, and emission data. 141 142 143

144

- **Meteorological inputs:** MOCAGE being an off-line model, it receives its meteorological fields from an independent weather model, every 3 or 6 hours. The fields generally come from the IFS model, from the ARPEGE model or from ERA-INTERIM [22] and more recently ERA5 [23] reanalyses. 145 146 147 148
- **Atmospheric composition :** MOCAGE describes the chemical composition of the atmosphere on 47 vertical levels from the surface up to 5 hPa, with a resolution of 40 m to 800 m at the top of the stratosphere. The horizontal resolution can vary from local scale ($0.1\,^{\circ} \times 0.1\,^{\circ}$) to regional ($0.5\,^{\circ} \times 0.5\,^{\circ}$) up to global domain with 1 or 2°. The model was initially developed for gaseous species (112 species implemented), whose processes and interactions are described in [24]. The Primary Aerosols (PA) were implemented by [25] for 4 species : the Desert Dust, the Sea Salts (SS) and the Black and Organic Carbons (BC, OC). Their description was improved by [26], in particular in the description of deposits, and with the development of the aerosols DAS. The inorganic aerosols were implemented by [27], namely nitrates, sulfates and ammonium. The large-scale transport, which corresponds to the atmospheric circulation (advection) is calculated thanks to the meteorolical fields. Then, the finer resolution processes (convection, turbulent diffusion) are solved from sub-mesh parameterizations (more details in [28]). 149 150 151 152 153 154 155 156 157 158 159 160 161 162

- **Emissions :** Emissions are the sources of pollutants in the atmosphere. They can be determined by emission inventories (anthropogenic, biogenic sources...), or by dynamic emission for some particles pulled from the surface following a natural forecast (DD, SS). The main emissions inventories are MACC-City [29] for anthropogenic pollutants, MEGAN-MACC [30] for biogenic emissions and methane, or GEIA for the NOx [31]. The dynamic emissions are calculated with a parametrizations via the meteorological parameters listed above. These parametrizations take into account the surface properties (composition, roughness...) and determine the necessary conditions (in general wind force and direction) to pull out a calculated quantity of particles.

In addition to these 3 elementary inputs, the model equations can be constrained from observations via the MOCAGE-Valentina DAS [32,33] validated for the assimilation of aerosol observations from imager such as MODIS [34] and lidar instruments [35]. This technique aims to combine the high spatial and temporal resolution of the model with the good accuracy and the specific coverage of the observations.

2.2.2. Validation of the NR with AERONET in-situ observations

To ensure that the NR is a good representation of reality, we perform a comparative analysis in terms of AOD from the global AErosol RObotic NERwork (AERONET) in-situ observations. AERONET represents hundreds of groundbased sun photometers network, monitoring optical properties of aerosols from 340 up to 1020 nm. With a large spatial coverage and an accuraçy of ±0.01 for AOD at 550nm, it aims to validate CTM and satellite products for aerosol study [36]. We use level 1.5 datas on version 3 (https://aeronet.gsfc.nasa.gov, *last check : Novembre 2022*), with automatic cloud screening. Over the globe and for the simulated period of the NR, AERONET provides more than two million measurements with hourly resolution.

Such validation has already been performed in the work on the validation of the MODIS pre-operational AOD assimilation system in MOCAGE by [**?**] which will serve as a reference for this study. In this reference study, the comparison with AERONET showed for the year 2018 (year of the NR) relatively low biases and root mean square error (RMSE) with the exception of Central Africa and South East Asia. These regions are frequently affected by biomass fires and anthropogenic pollution episodes respectively, phenomena sometimes difficult to represent in the model. However, even in these regions the correlation is satisfactory with values above 0.7. For the years of 2018 (2019), average scores of reference for correlation, bias and Root Mean Square Error (RMSE) are about 0.781 (0.812), -0.01 (-0.007) and 0.128 (0.138) respectively.

For the current study, Figure 2 presents the spatial validation of the NR in terms of correlation, bias and RMSE at the global scale over the whole simulation period of the NR. The first thing we observe is the good quality of the model on all the statistics in the Europe/Mediterranean and USA/Canada regions where two of the three events analyzed in this study are located. Concerning the anthropogenic pollution event, this one is located over China and it is not well covered by the AERONET network. The lower scores in terms of bias and RMSE in this region (greater than 0.1, and 0.3, respectively) are however accompanied by a good correlation.

Figure 3 completes it with a scatter plot representing the set of AERONET observations in comparison with the NR. The average scores of correlation, bias and RMSE are about (differences with the 2018 reference) 0.781 (=), 0.026 (+0.036) and 0.138 (+0.01). These differences are of the same order of magnitude as the differences between the reference for 2018 and 2019, demonstrating the validity of the NR. We see a positive bias between MODIS assimilation and AERONET stations, strongly driven by the lower (more frequent) AOD values (lower than 0.2). The overestimation of MODIS observations compared to AERONET in terms of AOD has already been documented over continental surfaces (e.g.:

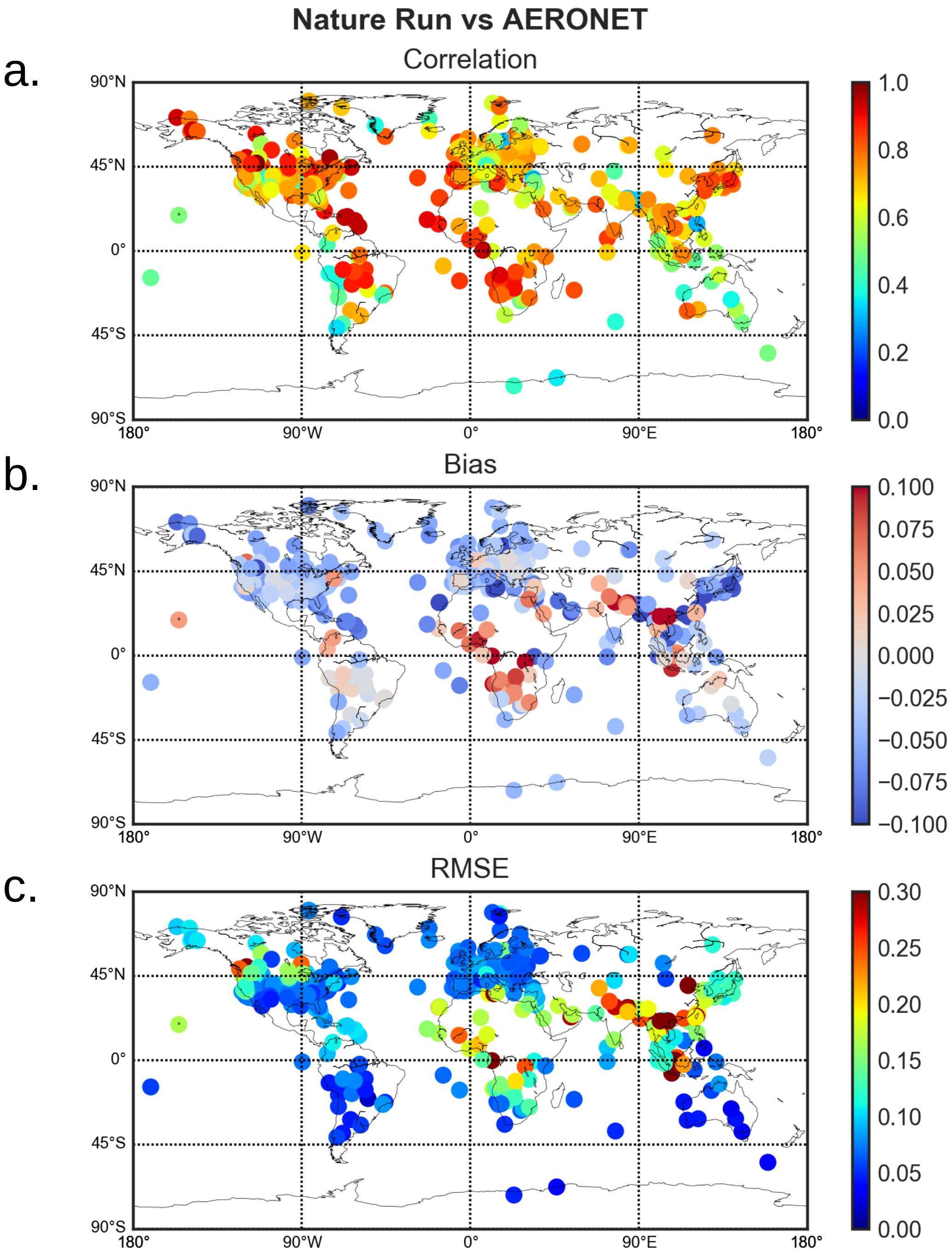

Figure 2. Maps of comparison between the NR and the AERONET in-situ Observations in terms of AOD over the globe and from 01, February, 2018 to 31, Septembre, 2018. Statistics are performed in terms of (a): Correlation, (b): Bias and (c): RMSE.

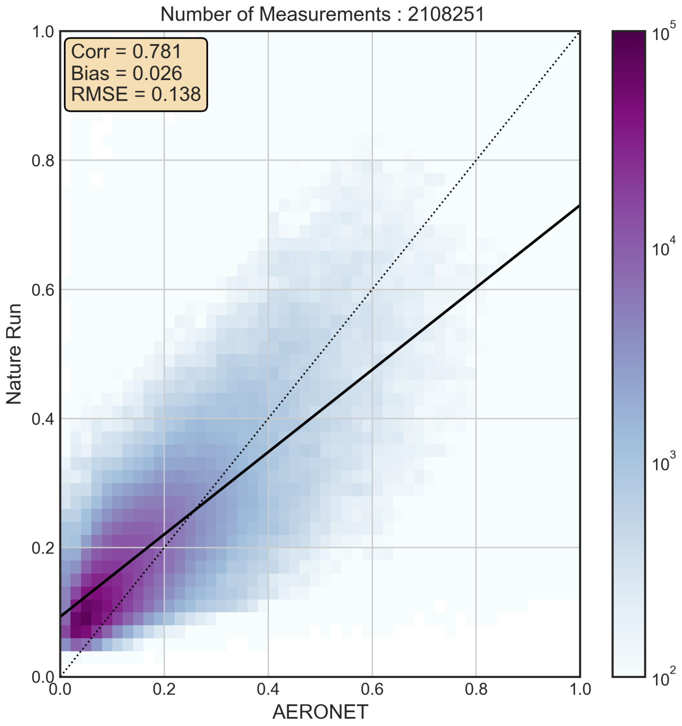

Figure 3. Scatter plot of AERONET vs NR in terms of AOD from 01, February, 2018 to 31, Septembre, 2018.

[37]) for both the Aqua and Terra platforms. The main differences in terms of statistics between the NR and the reference can be attributed to the duration of the simulation, which is shorter in the case of the NR, as well as to the initial state. 216 217 218

2.3. Inversion of the aerosol extinction and backscatter coefficients 219

2.3.1. The lidar equation 220

The backscatter coefficient β $(\mathrm{m}^{-1}\cdot\mathrm{sr}^{-1})$ of scatterers (such as particles and molecules), indicates the proportion of light scattered in the opposite direction of the incident photons. In the other hand, the extinction coefficient α (m^{-1}) represents the proportion of light absorbed or scattered in all other directions of the volume. These coefficients are key variables in the lidar equation, which connects the backscattered light power $\mathrm{P_{tot}}$ at the range r (directly linked with altitude z as $\mathrm{r} = \mathrm{z_{sat}} - \mathrm{z}$ for nadir pointing) for a fixed wavelength λ to the optical properties of the atmosphere. In its semi-complete version, this equation can be written as follows: 221 222 223 224 225 226 227 228

$$\mathrm{P_{tot}}(\mathrm{r}) = \frac{1}{r^2}\,\mathrm{K}\cdot\mathrm{G}(\mathrm{r})\cdot\left[\beta_{\mathrm{m}}(\mathrm{r}) + \beta_{\mathrm{p}}(\mathrm{r})\right]\cdot\exp\left[-2\int_0^r \left(\alpha_{\mathrm{m}}(\mathrm{r}) + \eta\alpha_{\mathrm{p}}(\mathrm{r})\right)\,\mathrm{dr}\right] \tag{1}$$

K and G(r) are related respectively to the instrument calibration and to its geometry and the overlap function between the laser beam and the telescope field of view, which do not involve intrinsic properties of the atmosphere. The extinction and backscattering coefficients are decomposed according to their molecular (m) and particulate (p) fraction. η, ranging from 0 to 1, is a term which corresponds to the multiple scattering coefficient. This coefficient modulates the phenomenon of light extinction by taking into account the ability of photons to reflect several times on neighboring aerosols when the density is 229 230 231 232 233 234 235 sifficiently high. We consider hereafter only simple scattering ($\eta = 1$). If the molecular parameters can be directly derived from meteorological profiles (pressure and temperature), the lidar equation still has two unknowns, which makes it unsolvable. On the other hand, the vertical structure of the atmosphere can directly be studied in qualitative terms using Attenuated Total Backscatter (ATB) profiles (see the equation below). However, this Level 1 (L1) product do not provide quantitative information nor indicator of the chemical composition of the atmosphere, which is necessary for a deep understanding about the interactions between aerosols and the environment.

$$\mathrm{ATB(r)} = \frac{\mathrm{S(r)}}{\mathrm{K \cdot G(r)}} = [\beta_\mathrm{m}(\mathrm{r}) + \beta_\mathrm{p}(\mathrm{r})] \cdot \exp\left[-2\int_0^r (\alpha_\mathrm{m}(\mathrm{r}) + \alpha_\mathrm{p}(\mathrm{r}))\,\mathrm{dr}\right] \tag{2}$$

With $\mathrm{S(r)} = \mathrm{r}^2 \cdot \mathrm{P_{tot}(r)}$ called the range-corrected lidar signal. For the following steps, the overlap function is assumed to be complete ($\mathrm{G}(r) = 1$). The aims of this section is to present the two aerosol inversion methods to retrieve the optical properties of the particles compared in this study. The first method is based on the classic inversion algorithm used for elastic backscatter lidars such as CALIOP, called hereafter Klett inversion algorithm. It has the instrumental advantage of requiring a single and simple detection system. However, this method requires an a-priori assumptions about the state of the atmosphere that can lead to large uncertainties. The second method with high spectral resolution avoids such assumptions by exploiting the Doppler shift phenomenon to separate the molecular component from the total signal. The challenge for both methods is to derive to the most accurate distance-dependent particle backscatter, extinction and lidar ratio profiles $\mathrm{LR_p}(r)$. This last one is defines as:

$$\mathrm{LR_p(r)} = \alpha_\mathrm{p}(\mathrm{r})/\beta_\mathrm{p}(\mathrm{r}) \tag{3}$$

2.3.2. Elastic backscatter lidar

The Rayleigh theory assumes a proportional relationship between the extinction and molecular backscatter coefficients of $8\pi/3$, which is not the case for particle coefficients, highly dependent on the shape, size and chemical composition of the elements. A first guess of $\mathrm{LR_p}$ can however be estimated by making an assumption on the observed particulate species, and from empirical measurements of aerosol properties [qq citations]. In a parallel way, $\mathrm{LR_m} = 8\pi/3$ is defined and independent of the range. From the ATB formula, and by replacing the extinction coefficients according to the different lidar ratio and backscatter coefficients, we obtain the following equation :

$$\begin{aligned}\mathrm{LR_p(r)} \cdot \mathrm{ATB(r)} \cdot \exp\left[-2\int_0^r (\mathrm{LR_p(r)} - \mathrm{LR_m})\beta_\mathrm{m}(\mathrm{r})\,\mathrm{d}r\right] \\ = \mathrm{Y(r)} \cdot \exp\left[-2\int_0^\mathrm{r} \mathrm{Y(r)}\,\mathrm{dr}\right]\end{aligned} \tag{4}$$

Where Y(r) is an introduced term of the form :

$$\mathrm{Y(r)} = \mathrm{LR_p(r)} \cdot [\beta_\mathrm{p}(\mathrm{r}) + \beta_\mathrm{m}(\mathrm{r})] \tag{5}$$

At this point, it is reported that all the terms in the left-hand side of the equation 4 are known or assumed (i.e. $\mathrm{LR_p}$). In the right-hand side β_p remains unknown. By putting each member to the logarithm, and applying a derivative with respect to r, we obtain the following equation:

$$\frac{\mathrm{d}}{\mathrm{d}r}\left[\ln\left(\mathrm{S(r)}\cdot \mathrm{LR_p(r)}\cdot \exp\left[-2\int_0^r (\mathrm{LR_p(r)}-\mathrm{LR_m})\beta_{\mathrm{m}}(\mathrm{r})\,\mathrm{d}r\right]\right)\right] = \frac{1}{\mathrm{Y(r)}}\cdot\frac{\mathrm{dY(r)}}{\mathrm{d}r}-2\mathrm{Y(r)}^2 \quad (6)$$

Equation 6 is of the type of Bernoulli's differential equation expressed in [38]. The solution is given from the initial condition $\mathrm{Y}(r_0) = \mathrm{LR_p}[\beta_{\mathrm{p}}(r_0)+\beta_{\mathrm{m}}(r_0)]$, with $r_0 = r_{ref}$, for the retrieval application, where we can consider $\beta_{\mathrm{p}}(r_0) \ll \beta_m(r_0)$ (i.e. an aerosol free atmosphere). The altitude of reference is often chosen at the top of the troposphere for wavelength inferior to 700 nm. The total backscatter coefficient profile $\beta_{tot}(r)$ (particular + molecular) is then:

$$\beta_{tot}(\mathrm{r}) = \frac{\mathrm{S(r)}\cdot\mathrm{Q(r)}}{\frac{\mathrm{ATB}(r_{ref})}{\beta(r_{ref})}-2\left(\int_{r_{ref}}^{r}\mathrm{LR_p(r')}\cdot\mathrm{ATB(r')}\cdot\mathrm{Q(r')}\,\mathrm{dr'}\right)} \quad (7)$$

With:

$$\mathrm{Q}(x) = \exp\left[-2\int_{r_{ref}}^{x}(\mathrm{LR_p}(x)-\mathrm{LR})\beta(x)\,\mathrm{d}x\right] \quad (8)$$

Finally, we can retrieve first order solutions of optical coefficients, with an assumption of the lidar Ratio fixed independent of the range:

- $\beta_{\mathrm{p}}(r) = \beta_{tot}(r)-\beta(r)$
- $\alpha_{\mathrm{p}}(r) = \mathrm{LR_p}(r)\beta_{\mathrm{p}}(r)$

From this first-oder solution, a range-dependant Lidar Ratio profile can then be determined, and implemented in equation 4 to 8 in a second iteration (or more) to better retrieve estimated aerosol properties [11,39].

The difficulty of the Klett inversion method is the definition of the correct LR first guess. As mentioned above, the LR variations depend on the microphysical properties of aerosols, their size, shape, but also the humidity profile. For the same family of aerosols, the LR can vary greatly depending on the area of emission. This is the case for example for desert dust with regional variability ranging from 35 to 60 sr [40]. Finally, the LR variability can also be observed along the vertical, either with distinct layers of different particulate species, or in-homogeneous mixtures. For the same species or for a well-mixed layer, the LR can also vary along the vertical via the humidity profile [41]. CALIOP's LR selection algorithm relies on an aerosol speciation technique based on surface type, layer height, and column-wide integrated ATB [40]. The algorithm allows for the specification of 11 aerosol species, including 7 in the troposphere. The different LR values for each tropospheric aerosol family are summarized in Table 1.

Table 1. Empirical LR for different aerosol species used in the CALIOP inversion algorithm in its version 4 at 532 nm and 1064 nm.

LR (sr)	CM[1]	DD	PC[2]/S[3]	CC[4]	PD[5]	DM[6]	ES[7]
532 nm	23 ± 5	44 ± 9	70 ± 25	53 ± 11	55 ± 22	37 ± 15	70 ± 16
1064 nm	23 ± 5	44 ± 13	30 ± 14	30 ± 17	48 ± 24	37 ± 15	30 ± 18

[1] Clean Marine, [2] Polluted Continental, [3] Smoke, [4] Clean Continental, [5] Polluted Dust, [6] Dusty Marine, [7] Elevated Smoke

2.3.3. High Spectral Resolution Lidar

In the atmosphere, the scatterers move by random agitation, responsible for a shift between the incident wavelength and the scattered wavelength (Doppler shift). The signal captured by the detector presents therefore a spectral length larger than the emitted one. The molecules are animated by Brownian motion characterized by speeds of the order of around 300 $\mathrm{m \cdot s^{-1}}$, when the agitation of aerosols is mainly driven by wind (around 10 $\mathrm{m \cdot s^{-1}}$) and turbulence (around 1 $\mathrm{m \cdot s^{-1}}$). The resulting spectrum clearly shows two distinct diffusion regimes [42]. The first one from particular scattering is very intense and narrow. It is characterized by a frequency shift between 3 and 30 MHz and is most likely similar to the initial spectral length. The second one, more Gaussian, has a width at mid-height of the order of GHz, typical of Rayleigh regime. By applying a suitable filter, it is possible to discriminate the molecular or particulate fraction of the signal into two different detectors. lidar equation of each channel can be formulated as follows relating to Attenuated Molecular Backscatter (AMB) or Attenuated Particular Backscatter (APB):

$$\mathrm{AMB}(r) = \beta_{\mathrm{m}}(r) \cdot \exp\left[-2\left(\int_0^r (\alpha_{\mathrm{m}}(r) + \alpha_{\mathrm{p}}(r))\ \mathrm{d}r\right)\right] \tag{9}$$

$$\mathrm{APB}(r) = \beta_{\mathrm{p}}(r) \cdot \exp\left[-2\left(\int_0^r (\alpha_{\mathrm{m}}(r) + \alpha_{\mathrm{p}}(r))\ \mathrm{d}r\right)\right] \tag{10}$$

In theory, the determination of the AMB signal and the APB relies on only one laser for deriving the lidar backscatter ratio R_β (Equation **??**) and then for estimating the backscatter coefficient without any a-priori information (Equation **??**). In practice, the determination of the variables is highly dependent on many factors such as the nature of the filter, its bandwidth, an accurate estimation of the cross talk bewteen channels and a good match between the laser frequency and the filter center frequency.

$$\mathrm{R}_\beta(r) = \frac{\mathrm{AMB}(r) + \mathrm{APB}(r)}{\mathrm{AMB}(r)} \tag{11}$$

$$\beta_{\mathrm{p}}(r) = (\mathrm{R}_\beta(r) - 1) \times \beta_{\mathrm{m}}(\mathrm{r}) \tag{12}$$

On the other hand, the extinction coefficient is determined from the derivative over distance of the logarithm of the ratio between the molecular density of the atmosphere $\mathrm{N_{atm}}$ (estimated) and the molecular signal AMB (filtered/measured) (Equation 13. This estimation is therefore more sensitive than the inversion of the backscatter coefficient [43]. Such sensitivity is unfortunate because the extinction determines how much light enters the atmosphere and is absorbed by the atmosphere that is the central key to study the impact of aerosols on the climate.

$$\alpha_{\mathrm{p}}(\mathrm{r}) = \frac{1}{2}\frac{\mathrm{d}}{\mathrm{dr}}\left(\ln\left[\frac{\mathrm{N_{atm}}(\mathrm{r})}{\mathrm{AMB}(\mathrm{r})}\right]\right) - \alpha_{\mathrm{m}}(\mathrm{r}) \tag{13}$$

Again, these first-order solutions provide a distance-dependent lidar Ratio profile but with much better accuracy. This $\mathrm{LR_p}(\mathrm{r})$ profile can be injected in turn into equation 7 to solve the lidar system, as with the previous method. It is worth nothing that in the present study, we focus in the estimation of aerosol backscatter profiles which have a straight forward formulation (Equations 11, 12). It does not need the calculation of derivatives of noisy signal, as it is the case for the aerosol extinction profile determination, which is not straight-foreward and will be tackled in future work.

2.3.4. SO Simulation setup

BLISS is an end-to-end Backscattering lidar simulator developed by the CNES in the framework of the MESCAL (Monitoring the Evolving State of Clouds and Aerosol Layers) phase 0 (pre-studies for AOS lidar definition). From all the inputs mentioned, it provides as outputs the signal received by a backscattering spaceborne lidar (level 0 and level 1 signals, including instrumental noise) and level 2 aerosol and cloud products (particle extinction and backscatter profiles). It simulates lidar instruments with a given filter properties file using HSRL, or Klett configuration with a particular LR profile. BLISS is based on the lidar equations as presented in [44]. BLISS is a modular software. In a simplified way, a first module (Scene Module) allows the calculation of the optical coefficients from the definition of the scene. A Signal Module computes then the calculation of the optical power from scene coefficients through lidar equation and conversion in electric signal. A third module (L1 Processing) is designed for the determination of the attenuated lidar signal (ATB, AMB, APB...). Finally, a last module (L2 Processing) inverses the optical properties of the scene.

To create the SO, the NR is sampled along a typical trajectory of a satellite lidar instrument such as CALIOP. The satellite follows a sun-synchronous orbit characterized by an average of two daytime (ascending) and two nighttime (descending) orbits. The solar zenith angle of each scene is computed from the the space-time coordinates. The surface properties (roughness and albedo) are determined from the ECOCLIMAP database at a resolution of $1^\circ \times 1^\circ$ (NR resolution). All simulations are made under the assumption of a clear sky without cloud cover (this aspect will be analyzed in future work). The NR atmospheric profiles are extracted in terms of extinction and particle backscatter at 532 nm at a from the surface up to $\sim$ 14 km altitude. Observations are averaged with a resolution of 0.5° in latitude and longitude and thus horizontal resolution (distance along which the profiles are averaged) of SO are fixed to 50 km having a significant impact on the Signal-to-Noise-Ratio (SNR). Since the MOCAGE model does not estimate particle depolarization, we assume that all particles are spherical as a first approximation for estimating their optical properties. Although this is an approximation, the lidar ratios estimated by MOCAGE for non-spherical particles as desert dust is coughly consistent with literature (see section 3.1). At the simulator output, the total backscattered lidar power is considered equivalent to the ottal poxer detected on the parallel track. The corresponding meteorological profiles (pressure, temperature and humidity) and the ground altitude are directly taken from the CALIOP Level 2 (L2) products data in version 4.2 (https://www.icare.univ-lille.fr/, *last check November 2022*). All these inputs are then provided to the the BLISS lidar signal simulator together with instrumental parameters from Table 2 for both lidar configuration. As an example, the characteristics of the CALIOP lidar at 532nm are also noted. The parameters corresponding to the properties of the detectors (e.g. quantum efficiency) are provided with the software and correspond to the characteristics of a Photomultiplier Tube (PMT) for CALIOP and a Phototnis MicroChanel Plate (MCP-PMT-Photonis, [45]) for the two AOS configurations (indicated for 532 nm and 355 nm). In addition, the transmission coefficients of the HSRL matrix specific to the interferometer filter correspond to classical properties as envisaged in the AOS project.

Table 2. Instrumental characteristics of the CALIOP, AOS_Backscatter and AOS_HSRL lidars.

Parameter	CALIOP_Like	AOS_Backscatter	AOS_HSRL
Altitude (km)	705	450	450
Wavelenght (nm)	532	532	532
Emitted power (W)	2.2	8	8
Pulse duration (ns)	20	15	15
Repetition Frequency (Hz)	20	70	70
Telescope diameter	1	1	1
lidar LOS zenith angle (°)	3	3	3
Filter bandwith (nm)	0.63	0.1	0.1
HSRL filtrer	No	No	Yes

2.3.5. Overview of BLISS simulation in comparison with CALIOP observations

In order to analyze the performance of the BLISS software, this section presents comparisons between the NR, observations from CALIOP (L1, L2) and their equivalent simulation of CALIOP_like synthetic measurements using BLISS with instrumental parameters presented in the Table 2 (CALIOP_Like). For this example, we consider a region centered on the Mediterranean Sea, Southern Europe and Northern Africa (medit). This region is bounded by latitudes [50 ; 20] °N and longitudes [-20 ; 40] °E. It corresponds to a desert dust event that occured on 22 March 2018. The area of analysis is limited to that affected by this event so as to assume a $LR_p = 44.4$ sr as first guess, which is used as input of the simulator for desert dust L2 Klett inversion (Table 1).

Firstly, Figure 4 focuses on the observations (real and synthetic) of ATB at 532 nm. The figure is divided into three ATB transects that follow the CALIOP trajectory. The transect 4-a represents the ATB profiles calculated by MOCAGE (implemented by [46]). Blancks (no value) near the surface correspond to the orography. Several aerosol layers can be seen here, some of which can reach 8000 m in altitude and cover large distances. Each of these aerosol layers is present in the transect 4-b, representing the ATB observations of CALIOP. While the intensities in terms of attenuated backscatter may moderately differ, the vertical and horizontal extents of the aerosol layers depicted in the MOCAGE NR are similar to those shown by CALIOP real observations. In the CALIOP real transect, missing data above 1000 m mainly correspond to the presence of opaque clouds, which are not simulated by the MOCAGE setup used here. The Figure 4-c represents the same transect but for the SO from BLISS.

In both real and synthetic observation transects, we observe a transition from relatively low noise conditions to noisy signals (marked with the red line) and with similar variability associated to noise in both cases. This phenomenon corresponds to the transition between night and daytime measurements, where background sunlight is a source of instrumental noise. This shows that the noise simulated in CALIOP_Like is rather realistic both during day and night. This difference in noise intensity suggests that we expect a difference in terms of errors and possible divergence in the inverted particle backscatter profiles in the two cases.

Figure 5 is constructed in the same way as Figure 4 but represents the particle backscatter coefficient at 532 nm (obtained from Klett inversion in the case of CALIOP and CALIOP_Like transects in panels b anc c). Note that the resolution of the L1 and L2 products are not identical (respectively 70 m and 5 km), as well as the estimation of the ground height. The transects 5-a, 5-b and 5-c of β_p thus correspond to the NR, the CALIOP observation and the SO, respectively. As discussed in the previous sections, the inversion of the lidar signal by the Klett method relies on strong assumptions that can lead to large uncertainties. In agreement with the figure representing the ATB transects and with literature, Figure 5-b shows a significant number of missing or diverging values. The comparison of Figures 5-b and 5-c must be done with great care. First, the choice of CALIOP LR is based on a selection algorithm, which relies on the integrated measurement of ATB, surface properties, and depolarization (among others). In the case of Transect 5-c, the first guess is set to 44.4 sr. In addition to that, the reference altitude is also fixed in the case of the SO transect, at 10 km. At this altitude, we can see that the particle signal is clearly not zero and may correspond to particles of another species than desert dust.

The retrieved particular backscatter structures shown by CALIOP and CALIOP_Like differ more than in the case of ATB. However, the main structures of desert dust layers are similary depicted both in real and synthetic measurements, especially in terms of horizontal extent and maximum altitude.

In conclusion of this section, the comparison of ATB transects between NR, CALIOP and a simulation of CALIOP show good consistency of BLISS simulated signals. Simulated noise has the same order of magnitude of that in real measurements, both during day and night. A systematic overestimation of the simulated signal compared to the NR is calculated to be of the order of [0.5 to 0.2] $10^-6\ m^{-1} \cdot sr^{-1}$. The amount of simulated signal compared

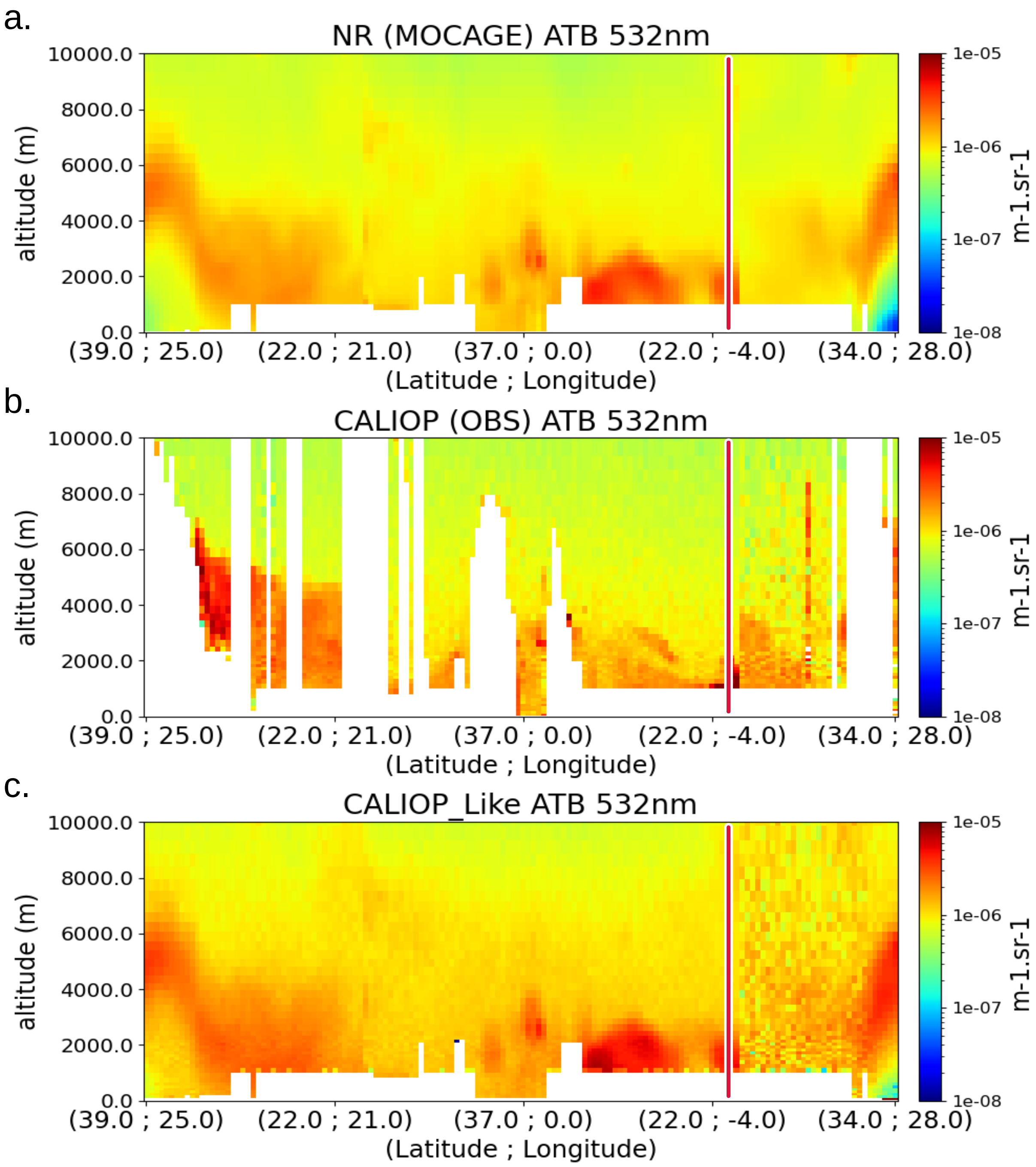

Figure 4. Comparison of ATB transects at 532 nm along the trajectory of CALIOP for the day of March, 22, 2018 over the medit region. (a): Transect from the NR, (b): CALIOP observations and (c): the corresponding CALIOP_Like SO. The vertical red line corresponds to the start of the daytime orbit (12:29 UTC).

Preprints (www.preprints.org) | NOT PEER-REVIEWED | Posted: 13 December 2022 doi:10.20944/preprints202212.0237.v1

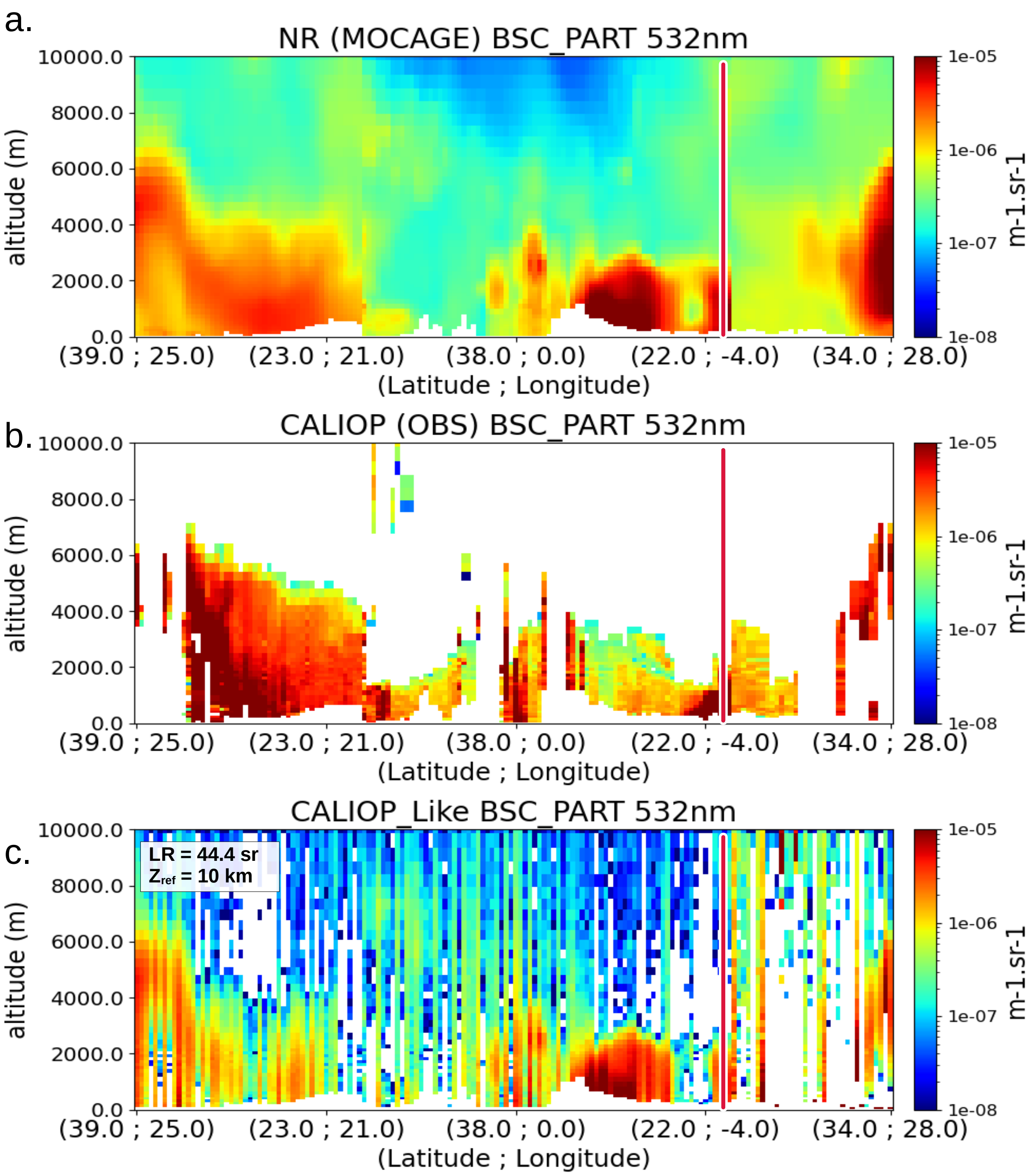

Figure 5. Same legend as figure 4 but for particular backscatter at 532 nm.

to the amount of measured signal affects the comparison of the level 2 products. The latter show more deviations from the NR for both Klett inversions. However, the inverted profiles from measured and simulated signals agree well in the average, especially in terms of variability. Therefore, the synthetic observations from BLISS show sufficient consistency so as to apply the same approach to different study cases and lidar configurations.

3. Results

The objective of this section is to illustrate the differences between AOS_Backscatter and AOS_HSRL SO for 3 case studies corresponding to different events (desert dust, wildfires and anthropogenic pollution). To account for the dependence of the Klett inversion method on an a-priori LR assumption, each scene focuses on a different aerosol species, which can be associated with one of the tropospheric aerosol families in the CALIOP classification algorithm (see Table 1).

3.1. The desert Dust event

Figure 6 shows an example of the added value of an AOS lidar configuration with HSRL compared to a standard (backscatter) configuration for a desert dust event. The panel (a) shows the horizontal distribution of the AOD from the NR corresponding to a desert dust transport event. The thick black line indicates the AOS lidar trajectory from north to south.

Figure 6-b represents the transect of backscatter profiles extracted from the NR following the trajectory of the instrument (in the X-axis are shown latitudes and longitudes) as shown in Figure 6-a. This Figure 6-b highlights clearly the plume of desert dust sampled by the instrument, with high values of the backscatter coefficient and a vertical extent reaching 8000 m at the northernmost point of the plume (latitudes between ∼40 °N and ∼30 °N).

This plume extends over a fairly large area (latitudes between ∼50 °N and ∼20 °N) with backscatter coefficients exceeding 10^{-5} $m^{-1} \cdot sr^{-1}$ and a vertical range of about 4000 m over this region. Figure 6-c shows the transect of lidar ratio profiles as astimated in the NR. The variability of the LR is rather limited especially within the desert dust plume (between 40 sr and 60 sr). These values of LR are consistend with the assumption of a LR of 44 sr used for the Klett inversion for this case study. It is also consistent with LR of desert dust considered in other studies ([47,48]).

Figure 6-d shows the transect of particle backscatter coefficient profiles derived from Klett inversion (using elastic backscatter lidar measurements, noted AOS_backscatter). The desert dust plume depicted by these inverted profiles are consistent with the NR in terms of the overall structure of plumes and the location of maximum and minimum values of particle backscatter coefficients. Nevertheless, the inverted particle backscatter profiles are relatively noisy and shown significant negative biases. These errors are highlighted in Figure 6-f where clear differences between the NR and AOS_backscatter are shown. The large bias (of the order of -80 %) is mostly negative for all backscatter profiles. This shows an underestimation of AOS_backscatter compared to the NR, mainly associated with the assumption of a aerosol free altitude at 10 km for normalization and differences between the assumed and actual LR.

On the other hand, clearly better performance is found for particle backscatter profiles derived from the inversion of lidar measurements using HSRL technology (Figure 6-e (AOS_HSRL)). This figure shows that the inverted profiles are in very good agreement with the NR profiles, with a good localization of the desert dust plume and with almost the same vertical range and particles backscattering values. The difference between AOS_HSRL and NR (Figure 6-g) shows that errors in the AOS_HSRL retrieval are random, and very little mean biases. The point-to-point differences between the two datasets is oscillate generally between -10 and 15 %. The results from this figure clearly illustrate the added-value of HSRL measurements for a better characterization of the vertical distribution of desert dust aerosol.

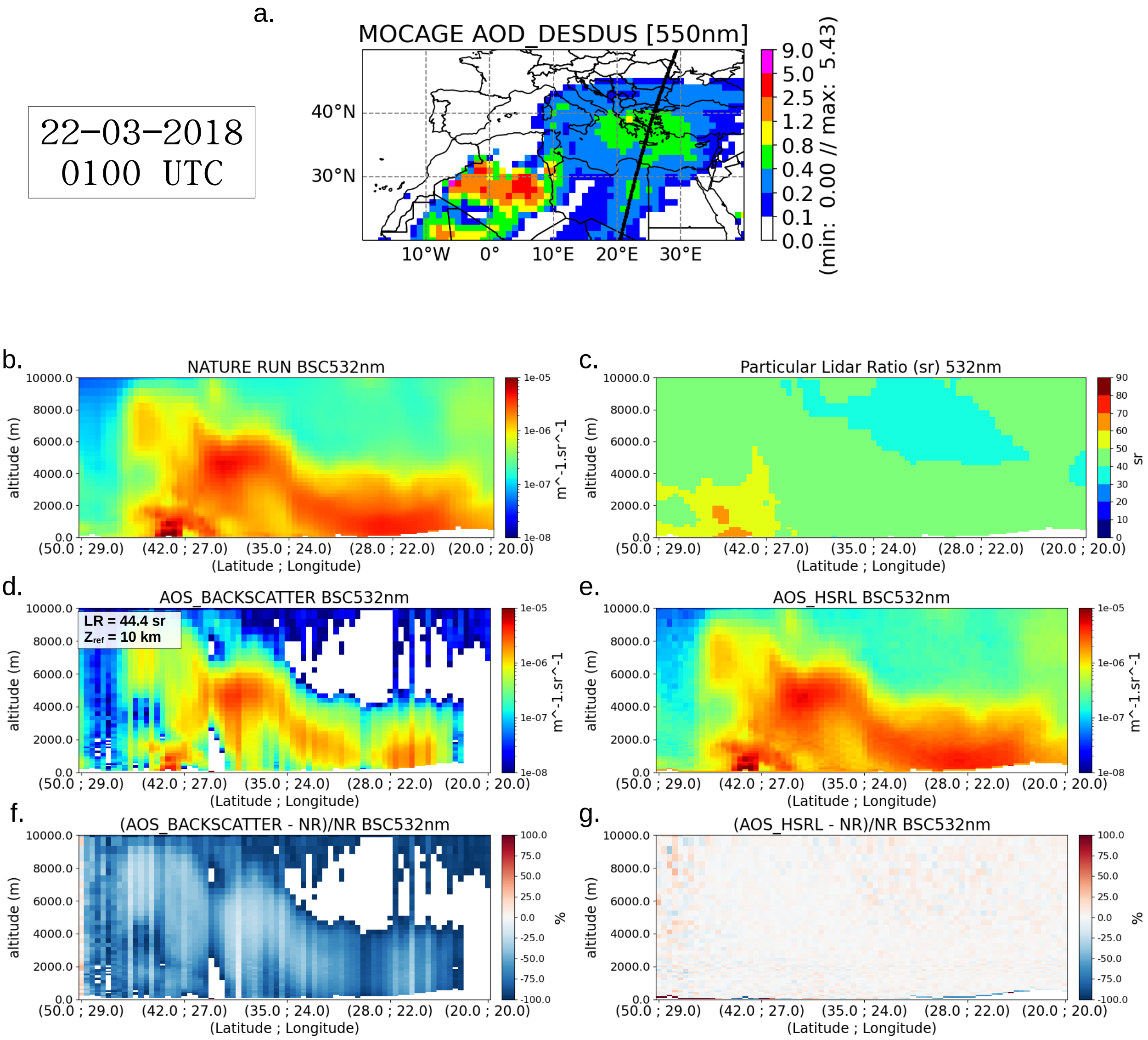

Figure 6. Case of the 22 of March 2018 at 0100 UTC. (a): AOD of DD from the NR together with the studied satellite trajectory (black line). (b): Particular backscatter profiles transect of a desert dust outbreak along the satellite trajectory in the NR. (c): Corresponding particular lidar Ratio transect calculated from the NR. (d, e): Simulation of the backscatter coefficient SO for the AOS_Backscatter and the AOS_HSRL configurations. (f, g): Relative mean bias (SO-NR)/NR of both instruments.

3.2. The Wildfire event

The second case shown in Figure 7 describes a wildfire event located on the west coast of Canada. The satellite follows a southward trajectory, sampling the thick dense smoke plume at the latitude of ∼47 °N at 1200 UTC as can be seen in Figure 7-a (in this case, the AOD of Organic Carbons (OC) is represented). The transect shown the vertical distribution of the smoke layers is seen in Figure 7-b, with the densest plume reaching 4000 m. Figure 7-c shows the corresponding transect of lidar ratio, displaying values between 50 sr to 60 sr over the northern part of the plume (up to latitude ∼41 °N) and between 60 sr to 70 sr at its center. These values are consistent with observations of other biomass burning events, such as a LR of 70 ± 25 reported in [40]. We also consider 70 sr as assumption for the Klett algorithm for this event, and the reference altitude is set to 10 km.

Around ∼40 °N, the satellite is above the sea surface and no longer observes the smoke plume. This is shown both on the map, and on the LR transect where the ratio drops down to 30 sr, far from the uncertainty allowed for the choice of the Klett assumption in the case of biomass burning. In this area, the most intense layer, close to the surface, is therefore relatively far from the reference altitude.

The result of the AOS_Backscatter lidar inversion shows a good retrieval of the vertical structure of the densest part of the smoke plume (errors in AOS_Backscatter of ∼ 10 %, bounded by latitudes [∼55 °N; ∼41 °N]. The maximum altitude of this part of the plume is about 4000 m. Secondary smoke plumes are also identified, although their particle backscatter coefficients are underestimated and significant errors are apparent. A characteristic artifact of the Klett inversion can be seen in the center of the plume. The inverted backscatter profiles diverges for large values near the surface, leading to large overestimations, or invalid retrievals. This occurs when the denominator of equation **??** is near zero.

This dense smoke plume around 40 ° N, also shows the lowest errors for AOS_HSRL lidar (between -5% and 5%). The stable and assumption free HSRL inversion method was not penalized by the high values of particle backscatter coefficients. In contrast with respect to the Klett derived profiles, the HSRL approach is capable of observing the whole scene. All secondary smoke plumes are well observed by AOS_HSRL, as well as the thin aerosol plume near the surface over the ocean (with errors between -15 % to 15 %).

Still in the case of AOS_HSRL, the retrieval of aerosol backscatter profiles show larger errors over the notrhern part of the smoke plume (exceeding 40%), and globally everywhere oscillating between -30% and 30% when the backscatter falls below 10^{-7} $m^{-1} \cdot sr^{-1}$. This phenomenon may be apparent for low particle backscatter conditions and larger instrumental noise [49].

3.3. Urban pollution event

The last case concerns a large anthropogenic pollution event over western China. (see Figure 8). This region is concerned by frequent anthropogenic pollution episodes in winter in terms of particulate matter of diameter less than 2.5 μm (PM2.5) as well as PM10, SO_2 and NO_2 as reported by [50]. They report a 24-hour average concentrations of 100 $\mu g.m^{-3}$ (PM2.5), 160 $\mu g.m^{-3}$ (PM10), 40 $\mu g.m^{-3}$ (SO_2) and 60 $\mu g.m^{-3}$ (NO_2) averaged over the months of February from 2017 to 2019. Figure 8-a effectively highlights a significant nitrate aerosol event (maximum AOS of 1.81) sampled by the satellite at 0600 UTC (ascending orbit). The particle backscatter transect shows a very dense structure at low altitude (between 0 and ∼ 2 km), up to ∼ 6000 m towards ∼40 °N. Up to an average of 5000 m, Figure 8-c indicates that the LR is located between 50 sr and 60 sr with 70 sr for the densest part of the plume. We assume a LR first guess of 70 sr for this Polluted Continental type aerosols [40].

Figure 8-d clearly depicts saturated Klett inverted profiles at the lowest part of the dense aerosol layers (around 36 ° N). This transect is similar to the case study of [51] (in terms of aerosol extinction coefficients) which shows the difficulty of CALIOP to depict the full vertical extent of dense aerosol layers as compared to an airborne HSRL lidar following the same trajectory. Positive saturation at the lowest edge of the aerosol plume can exceed

doi:10.20944/preprints202212.0237.v1

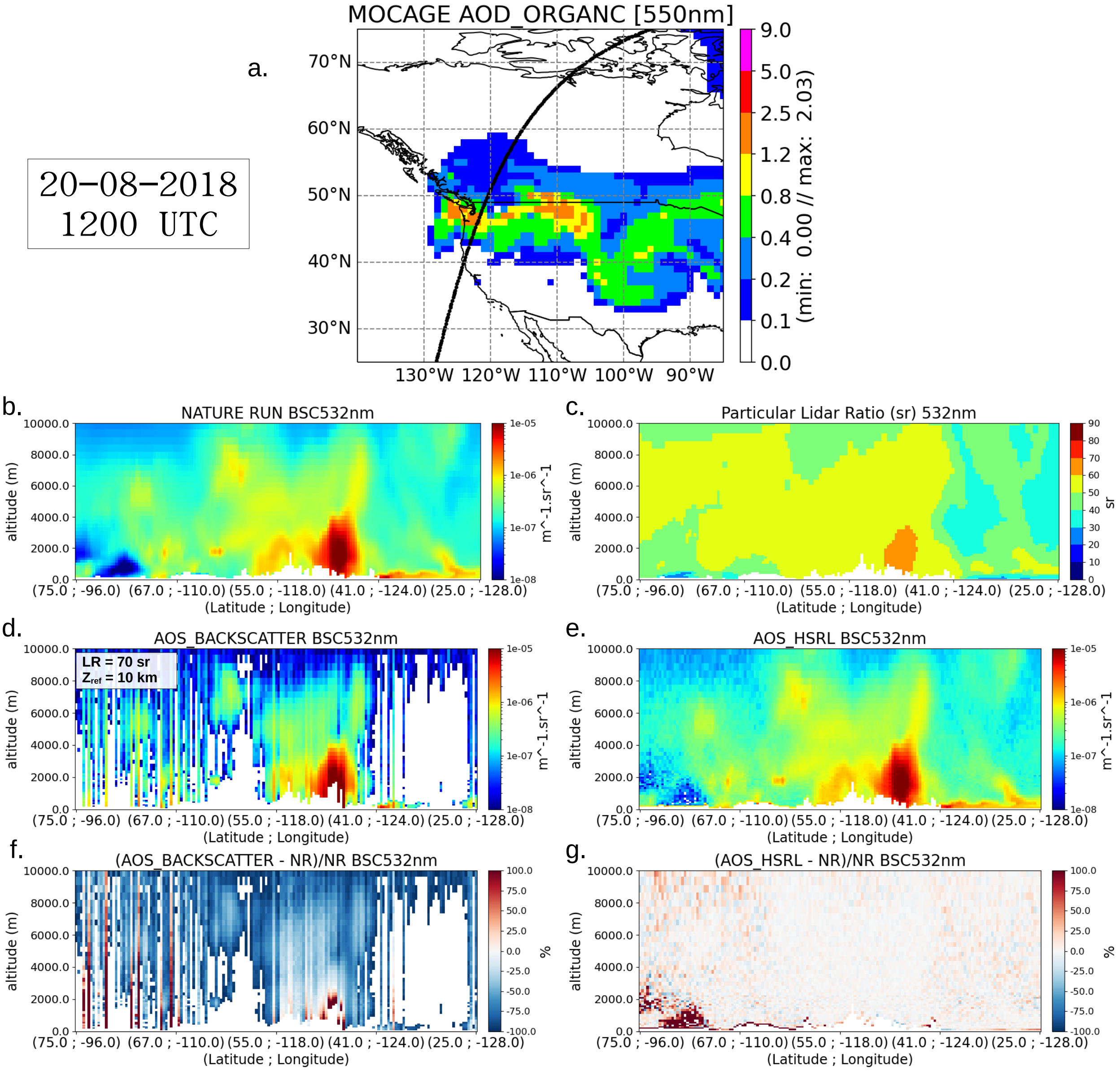

Figure 7. Same legend as figure 6 but for an wildfire event over Canada the 20 of August 2018 at 1200 UTC. The AOD of Organic Carbon from the NR is represented in (a).

± 150 % of relative bias (Figure 8-f). This panel also shows the limitations of the inversion method south of ∼36 °N latitude from 2000 to 10000 m up, where the LR of the NR is rather between 30 sr to 50 sr. The poor Klett estimation of the backscatter profile of this region can also be explained by the choice of z_{ref} at an altitude where the particle backscatter is clearly not zero ($\sim 5.10^7 \text{ m}^{-1} \cdot \text{sr}^{-1}$) as compared to the northern latitudes where the inversion is more efficient.

Figure 8-e and 8-g show the good ability of the HSRL method to invert all the aerosol layers as in the two previous cases. In the whole region where the particle backscatter is greater than $\sim 10^7 \text{ m}^{-1} \cdot \text{sr}^{-1}$, the error is around ±5 %. The relative deviation from the NR exceeds 40 % for the points with maximum plume altitude near the surface, and in the region with low particle content for the same reason given in the previous case.

This case summarizes the critical aspect of the good choice of first guess for the Klett inversion and the altitude at which the molecular signal is considered to be very large before the particle signal.

3.4. Overall performance of AOS_Backscatter and AOS_HSRL lidars

To draw conclusions with a larger temporal representativity than single transects, the experiment of the desert dust event is performed over a longer period. The SO are made from 20 to 25 March 2018, a period that covers most of the dust event. This represents ∼ 20 orbits and ∼ 1700 profiles at 0.5 ° × 0.5 ° resolution spread over the 5 days of analysis. This episode is selected because atmospheric conditions remains rather stable. Over this region, the variability of the LR profiles is rather stable over the whole period, both during the day and at night. This feature limits the contribution of bias during the inversion of elastic backscatter observations. The backscatter profiles are averaged and presented in Figure 9-a, as is the NR. The respective standard deviations are presented in Figure 9-b. In agreement with the three case studies presented previously, the deviations between NR and AOS_HSRL are very small in comparison with AOS_Backscatter. Figure 9-c represents the Relative Mean Bias (RMB) profiles. Ground echo simulated by BLISS for each profile are removed by not considering first levels above the surface. The mean bias is estimated to $1.10 \cdot 10^{-10}$ ($\text{m}^{-1} \cdot \text{sr}^{-1}$) (that represents 1.19 % of RMB) from ∼ 500 m up to the maximum altitude of simulation. In contrast, the AOS_Backscatter is characterized by an underestimation of around $-3.53 \cdot 10^{-9}$ ($\text{m}^{-1} \cdot \text{sr}^{-1}$) (that represents ~ -36.13 % of RMB), with a decreasing with altitude. The shape of the RMSE profiles in Figure 9-d highlights the vertical distribution of errors of the HSRL method, especially at low altitude (under 4000 m) through more intense plumes. The AOS_HSRL average RMSE is equal to $3.15 \cdot 10^{-7}$ ($\text{m}^{-1} \cdot \text{sr}^{-1}$) under 4000 m and equal to $1.83 \cdot 10^{-7}$ ($\text{m}^{-1} \cdot \text{sr}^{-1}$) for the whole profile against $2.21 \cdot 10^{-6}$ ($\text{m}^{-1} \cdot \text{sr}^{-1}$) and $1.38 \cdot 10^{-6}$ ($\text{m}^{-1} \cdot \text{sr}^{-1}$) for the AOS_Backscatter SO respectively.

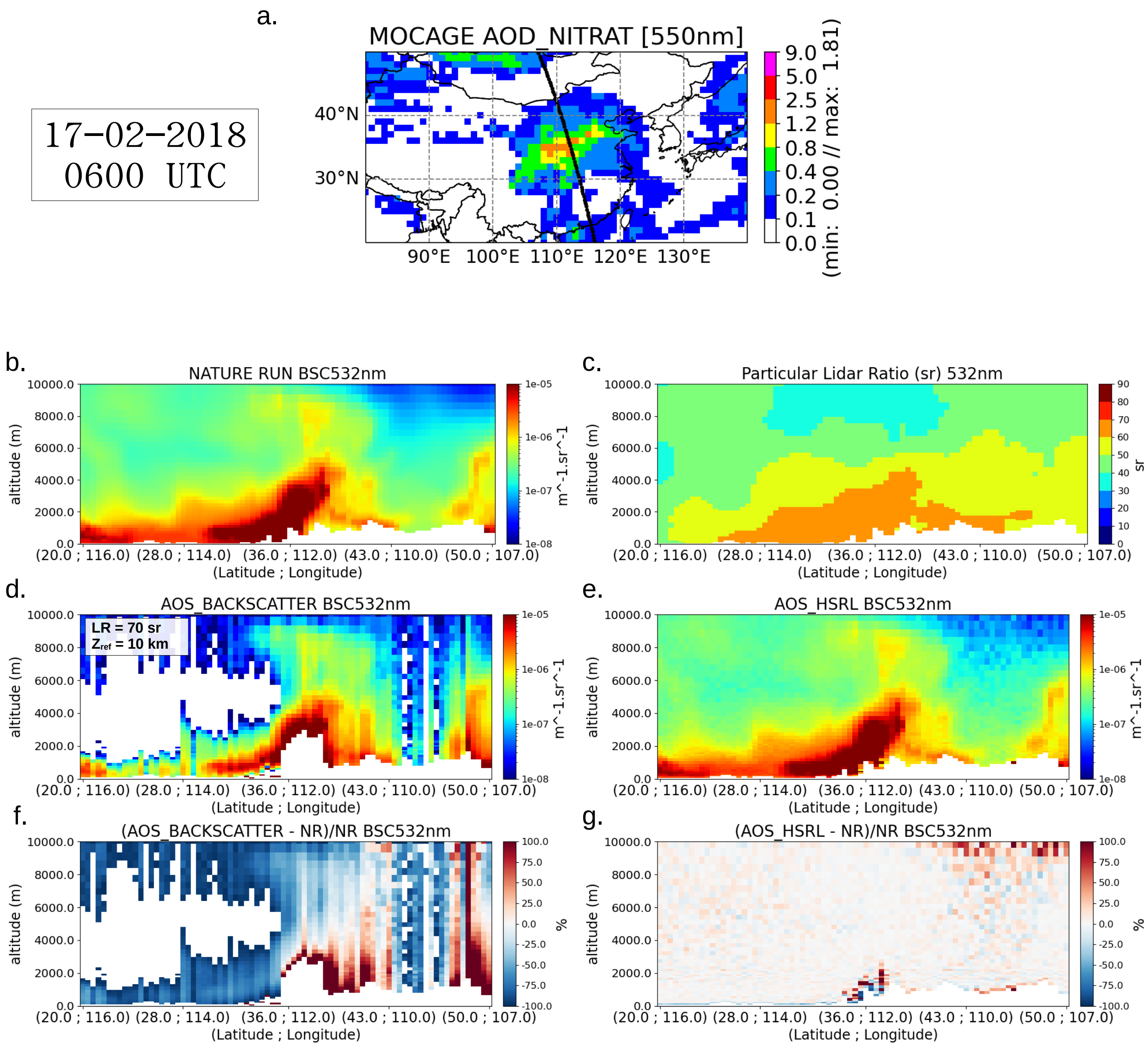

Figure 8. Same legend as Figure 6 but for an urban pollution event over China the 17 of March 2018 at 0600 UTC. The AOD of nitrate from the NR is represented in (a).

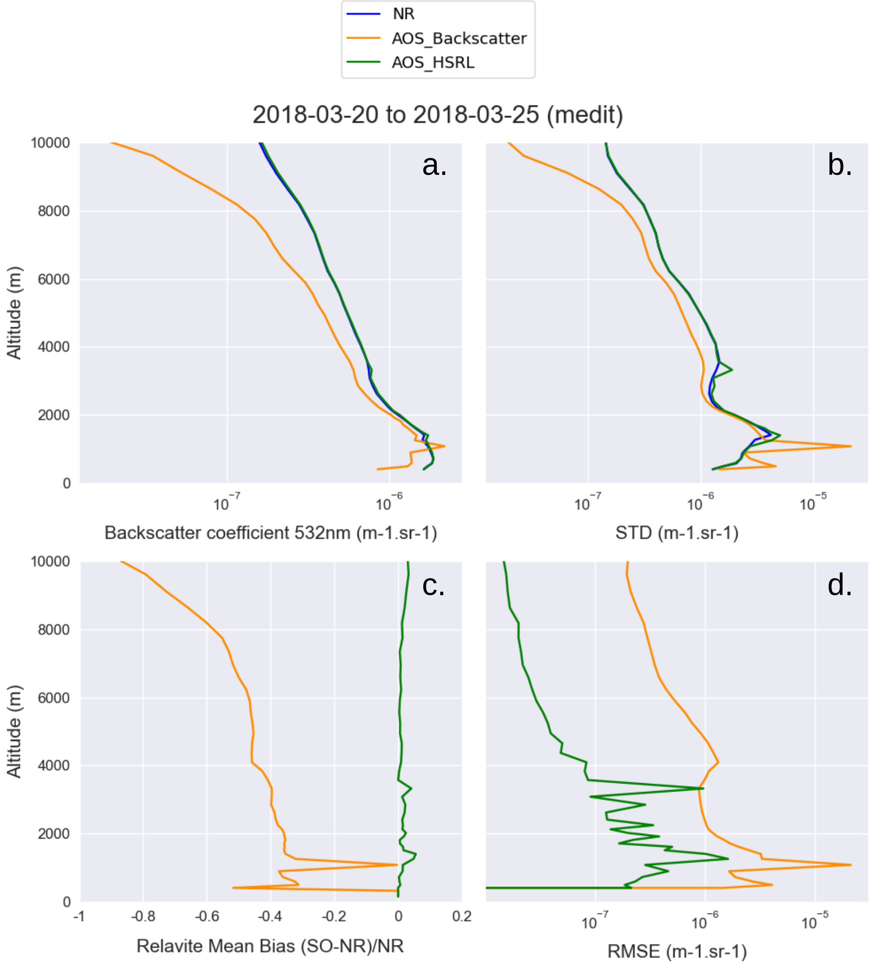

Figure 9. (a): Average profiles of particular backscatter coefficients at 532 nm from the NR (blue), the AOS_Backscatter SO (orange) and the AOS_HSRL SO (green) from March 20, 2018 to March 25, 2018 over the medit region. (b): Corresponding standard deviations profiles. (c): Relative Mean Bias (SO-NR)/NR of both instruments. (d): RMSE of both instruments versus the NR.

4. Conclusions and perspectives 574

In this study, we analyze the added-values of a HSRL spaceborne lidar with respect to 575 an elastic backscatter lidar, using a lidar signal simulator. A first part of analysis shows the 576 consistency of the SO in particular in term of ATB, as the simulator represents instrumental 577 noise in a similar way as CALIOP instrument real observations (considering different 578 backsground noise conditions). 579

We then build two sets of synthetic observations, considering the typical instrumental 580 parameters of the AOS mission, with or without HSRL. We compared the AOS for three 581 study cases, each time representing an orbit in a region centered on a dense aerosol episode. 582 In this way, the uncertainties on the choice of the first guess of Lidar Ratio for the classical 583 Klett inversion of backscatter lidar measurements are reduced. Each first guess was selected 584 based on the CALIOP inversion algorithm. In the case of the desert dust plume, with a fairly 585 uniform lidar ratio profile over the observed scene, we are able to study the contribution in 586 terms of inversion, with relative biases between -5 and +5% for the AOS_HSRL instrument 587 against -80% for the AOS_Backscatter instrument. A biomass fire18 shows the strong 588 impact of the lidar ratio choice especially when the satellite samples aerosols different from 589 smoke, with lower lidar ratio. In this case, the AOS_Backscatter observation diverges and 590 fails to detect the fine structure near the surface. Only the smoke plume is well represented, 591 contrary to AOS_HSRL observations that precisely characterize the whole scene in terms 592 of aerosol backscatter profiles. Finally, the third case study describes an anthropogenic 593 pollution episode, with a well identified lidar ratio profile over the entire event. This case presents the most densest plume in terms of backscatter coefficient of the three simulated scenes. The AOS_Backscatter instrument fails to invert the base of the aerosol layer. The synthetic observation shows important under- and over-estimations, exceeding 100%, where the AOS_HSRL observation shows good results on the whole event. In terms of relative bias, the HSRL lidar shows its greatest weaknesses when the signal becomes very weak, and the signal-to-noise ratio also decreases.

On average, the relative bias between the NR and the various synthetic observations is 1.19% (AOS_HSRL) and -36.13% (AOS_Backscatter). Regarding the RMSE, AOS_HSRL performs on average one order of magnitude better than AOS_Backscatter compared to NR.

The synthetic observations from AOS_HSRL can then be used to perform an Observing Simulation System Experiment (OSSE) [52] to evaluate the contribution of HSRL satellite lidar products to constrain a transport chemistry model. This type of aerosol OSSE experiments have been mostly performed for passive instruments [53] characterized by good horizontal coverage. Few have been performed for spaceborne aerosol lidars.

This configuration also allows to simulate the contribution of a potential UV channel in addition to the visible channel with or without HSRL, to see the added value of such a lidar for different aerosol species.

BLISS sofware availability

BLISS software is the property of CNES and has been registered with the Agency for the Protection of Programs. If compliant with AERIS platform's host conditions, it will soon be available on [https://www.aeris-data.fr/]. It is based on SAM software. The readers and reviewers interested in distribution of license, code or user manuals may contact CNES at the address affiliated in the list of co-authors.

Acknowledgements

We thank the Principal Investigators of AERONET and their staff for establishing and maintaining the sites used in this investigation.

Supplementary material: AOS Constellation

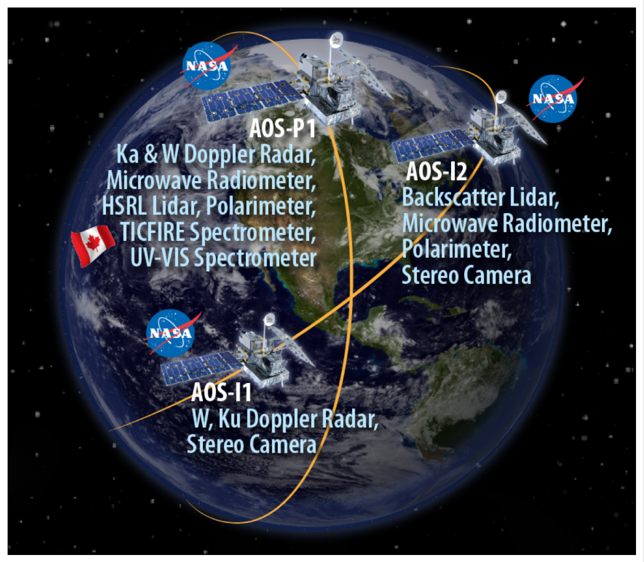

Figure 10. AOS satellites orbiting Earth (Atmosphere Observing System Community Assessment Report, https://aos.gsfc.nasa.gov/, *last check November 2022*).

References

1. WHO. *Ambient air pollution: a global assessment of exposure and burden of disease*; World Health Organization, 2016; p. 121 p.
2. Yu, H.; Chin, M.; Yuan, T.; Bian, H.; Remer, L.A.; Prospero, J.M.; Omar, A.; Winker, D.; Yang, Y.; Zhang, Y.; et al. The fertilizing role of African dust in the Amazon rainforest: A first multiyear assessment based on data from Cloud-Aerosol Lidar and Infrared Pathfinder Satellite Observations. *Geophysical Research Letters* **2015**, *42*, 1984–1991, [https://agupubs.onlinelibrary.wiley.com/doi/pdf/10.1002/2015GL063040]. https://doi.org/https://doi.org/10.1002/2015GL063040.
3. Boucher, O.; Randall, D.; Artaxo, P.; Bretherton, C.; Feingold, G.; Forster, P.; Kerminen, V.M.; Kondo, Y.; Liao, H.; Lohmann, U.; et al. Clouds and aerosols. In *Climate change 2013: The physical science basis. Contribution of working group I to the fifth assessment report of the intergovernmental panel on climate change*; Cambridge University Press, 2013; pp. 571–657.
4. Suzuki, K.; Takemura, T. Perturbations to Global Energy Budget Due to Absorbing and Scattering Aerosols. *Journal of Geophysical Research: Atmospheres* **2019**, *124*, 2194–2209, [https://agupubs.onlinelibrary.wiley.com/doi/pdf/10.1029/2018JD029808]. https://doi.org/https://doi.org/10.1029/2018JD029808.
5. Keil, A.; Haywood, J.M. Solar radiative forcing by biomass burning aerosol particles during SAFARI 2000: A case study based on measured aerosol and cloud properties. *Journal of Geophysical Research: Atmospheres* **2003**, *108*. https://doi.org/https://doi.org/10.1029/2002JD002315.
6. Su, T.; Li, Z.; Li, C.; Li, J.; Han, W.; Shen, C.; Tan, W.; Wei, J.; Guo, J. The significant impact of aerosol vertical structure on lower atmosphere stability and its critical role in aerosol–planetary boundary layer (PBL) interactions. *Atmospheric Chemistry and Physics* **2020**, *20*, 3713–3724. https://doi.org/10.5194/acp-20-3713-2020.
7. Chand.; R., W.; L, A.T.; K, S.S.; J, C.R. Satellite-derived direct radiative effect of aerosols dependent on cloud cover. *Nature Geosci* **2009**, *2*, 181–184. https://doi.org/https://doi.org/10.1038/ngeo437.
8. Winker, D.M.; Vaughan, M.A.; Omar, A.; Hu, Y.; Powell, K.A.; Liu, Z.; Hunt, W.H.; Young, S.A. Overview of the CALIPSO Mission and CALIOP Data Processing Algorithms. *Journal of Atmospheric and Oceanic Technology* **2009**, *26*, 2310 – 2323. https://doi.org/10.1175/2009JTECHA1281.1.
9. Winker, D.M.; Tackett, J.L.; Getzewich, B.J.; Liu, Z.; Vaughan, M.A.; Rogers, R.R. The global 3-D distribution of tropospheric aerosols as characterized by CALIOP. *Atmospheric Chemistry and Physics* **2013**, *13*, 3345–3361. https://doi.org/10.5194/acp-13-3345-2013.
10. Song, Q.; Zhang, Z.; Yu, H.; Ginoux, P.; Shen, J. Global dust optical depth climatology derived from CALIOP and MODIS aerosol retrievals on decadal timescales: regional and interannual variability. *Atmospheric Chemistry and Physics* **2021**, *21*, 13369–13395. https://doi.org/10.5194/acp-21-13369-2021.
11. Klett, J.D. Stable analytical inversion solution for processing lidar returns. *Applied Optics* **1981**, *20*, 211–220.
12. Fernald, F.G.; Herman, B.M.; Reagan, J.A. Determination of Aerosol Height Distributions by Lidar. *Journal of Applied Meteorology and Climatology* **1972**, *11*, 482 – 489. https://doi.org/10.1175/1520-0450(1972)011<0482:DOAHDB>2.0.CO;2.
13. Morancais, D.; Mazuray, L.; Barthès, J.C. ALADIN, the first wind lidar in space: development status. In Proceedings of the International Conference on Space Optics — ICSO 2006; Armandillo, E.; Costeraste, J.; Karafolas, N., Eds. International Society for Optics and Photonics, SPIE, 2017, Vol. 10567, p. 1056703. https://doi.org/10.1117/12.2308091.
14. Flamant, P.; Cuesta, J.; Denneulin, M.L.; Dabas, A.; Huber, D. ADM-Aeolus retrieval algorithms for aerosol and cloud products. *Tellus A: Dynamic Meteorology and Oceanography* **2008**, *60*, 273–286. https://doi.org/10.1111/j.1600-0870.2007.00287.x.
15. Illingworth, A.J.; Barker, H.W.; Beljaars, A.; Ceccaldi, M.; Chepfer, H.; Clerbaux, N.; Cole, J.; Delanoë, J.; Domenech, C.; Donovan, D.P.; et al. The EarthCARE Satellite: The Next Step Forward in Global Measurements of Clouds, Aerosols, Precipitation, and Radiation. *Bulletin of the American Meteorological Society* **2015**, *96*, 1311 – 1332. https://doi.org/10.1175/BAMS-D-12-00227.1.
16. Ansmann, A.; Müller, D. *Lidar and Atmospheric Aerosol Particles in Lidar: Range-Resolved Optical Remote Sensing of the Atmosphere*; K. Weitkamp editor, Springer-Berlag, New-York, 2005.

17. Braun, S.A.; Yorks, J.; Thorsen, T.; Cecil, D.; Kirschbaum, D. NASA'S Earth System Observatory-Atmosphere Observing System. In Proceedings of the IGARSS 2022 - 2022 IEEE International Geoscience and Remote Sensing Symposium, 2022, pp. 7391–7393. https://doi.org/10.1109/IGARSS46834.2022.9884029.
18. Burton, S.; Ferrare, R.; Hostetler, C.; Hair, J.; Rogers, R.; Obland, M.; Butler, C.; Cook, A.; Harper, D.; Froyd, K. Aerosol classification using airborne High Spectral Resolution Lidar measurements–methodology and examples. *Atmos. Meas. Tech.* **2012**, *5*, 73–98.
19. King, M.D.; Kaufman, Y.J.; Menzel, W.P.; Tanre, D. Remote sensing of cloud, aerosol, and water vapor properties from the Moderate Resolution Imaging Spectrometer(MODIS). *IEEE transactions on geoscience and remote sensing* **1992**, *30*, 2–27.
20. El Amraoui, L.; Plu, M.; Guidard, V.; Cornut, F.; Bacles, M. A Pre-Operational System Based on the Assimilation of MODIS Aerosol Optical Depth in the MOCAGE Chemical Transport Model. *Remote Sensing* **2022**, *14*. https://doi.org/10.3390/rs14081949.
21. Courtier, P.; Freydier, C.; Geleyn, J.; Rabier, F.; Rochas, M. The ARPEGE project at Météo France. In Proceedings of the Atmospheric Models, vol.2; Workshop on Numerical Methods, , 1991; pp. 193–231.
22. Dee, D.P.; Uppala, S.M.; Simmons, A.J.; Berrisford, P.; Poli, P.; Kobayashi, S.; Andrae, U.; Balmaseda, M.A.; Balsamo, G.; Bauer, P.; et al. The ERA-Interim reanalysis: configuration and performance of the data assimilation system. *Quarterly Journal of the Royal Meteorological Society* **2011**, *137*, 553–597, [https://rmets.onlinelibrary.wiley.com/doi/pdf/10.1002/qj.828]. https://doi.org/https://doi.org/10.1002/qj.828.
23. Hersbach, H.; Bell, B.; Berrisford, P.; Hirahara, S.; Horányi, A.; Muñoz-Sabater, J.; Nicolas, J.; Peubey, C.; Radu, R.; Schepers, D.; et al. The ERA5 global reanalysis. *Quarterly Journal of the Royal Meteorological Society* **2020**, *146*, 1999–2049.
24. Cussac, M. *La composition chimique de la haute troposphère : étude de l'impact des feux de biomasse et des processus de transports verticaux avec le modèle MOCAGE et les mesures IAGOS*; 2020.
25. Martet, M.; Peuch, V.H.; Laurent, B.; Marticorena, B.; Bergametti, G. Evaluation of long-range transport and deposition of desert dust with the CTM MOCAGE. *Tellus B* **2009**, *61*, 449–463.
26. Sič, B.; El Amraoui, L.; Marécal, V.; Josse, B.; Arteta, J.; Guth, J.; Joly, M.; Hamer, P. Modelling of primary aerosols in the chemical transport model MOCAGE: development and evaluation of aerosol physical parameterizations. *Geosci. Model Dev.* **2015**, *8*, 381–408.
27. Guth, J.; Josse, B.; Marécal, V.; Joly, M.; Hamer, P. First implementation of secondary inorganic aerosols in the MOCAGE version R2.15.0 chemistry transport model. *Geosci. Model Dev.* **2016**, *9*, 137–160. https://doi.org/10.5194/gmd-9-137-2016.
28. Josse, B.; Simon, P.; Peuch, V.H. Radon global simulation with the multiscale chemistry trasnport model MOCAGE. *Tellus* **2004**, *56*, 339–356.
29. Lamarque, J.F.; Bond, T.C.; Eyring, V.; Granier, C.; Heil, A.; Klimont, Z.; Lee, D.; Liousse, C.; Mieville, A.; Owen, B.; et al. Historical (1850-2000) gridded anthropogenic and biomass burning emissions of reactive gases and aerosols: Methodology and application. *Atmos. Chem. Phys.* **2010**, *10*, 7017–7039. https://doi.org/10.5194/acp-10-7017-2010.
30. Sindelarova, K.; Granier, C.; Bouarar, I.; Guenther, A.; Tilmes, S.; Stavrakou, T.; Müller, J.F.; Kuhn, U.; Stefani, P.; Knorr, W. Global data set of biogenic VOC emissions calculated by the MEGAN model over the last 30 years. *Atmospheric Chemistry and Physics* **2014**, *14*, 9317–9341. https://doi.org/10.5194/acp-14-9317-2014.
31. Yienger, J.J.; Levy II, H. Empirical model of global soil-biogenic NO emissions. *Journal of Geophysical Research: Atmospheres* **1995**, *100*, 11447–11464. https://doi.org/https://doi.org/10.1029/95JD00370.
32. Emili, E.; Barret, B.; Massart, S.; Le Flochmoen, E.; Piacentini, A.; El Amraoui, L.; Pannekoucke, O.; Cariolle, D. Combined assimilation of IASI and MLS observations to constrain tropospheric and stratospheric ozone in a global chemical transport model. *Atmos. Chem. Phys.* **2014**, *14*, 177–198. https://doi.org/10.5194/acp-14-177-2014.
33. El Amraoui, L.; Attié, J.L.; Ricaud, P.; Lahoz, W.A.; Piacentini, A.; Peuch, V.H.; Warner, J.X.; Abida, R.; Barré, J.; Zbinden, R. Tropospheric CO vertical profiles deduced from total columns using data assimilation: Methodology and Validation. *Atmos. Meas. Tech.* **2014**, *7*, 3035–3057. https://doi.org/10.5194/amt-7-3035-2014.
34. Sič, B.; El Amraoui, L.; Piacentini, A.; Marécal, V.; Emili, E.; Cariolle, D.; Prather, M.; Attié, J.L. Aerosol data assimilation in the chemical transport model MOCAGE during the TRAQA/ChArMEx campaign:

aerosol optical depth. *Atmospheric Measurement Techniques* **2016**, *9*, 5535–5554. https://doi.org/10.5194/amt-9-5535-2016.

35. El Amraoui, L.; Sič, B.; Piacentini, A.; Marécal, V.; Frebourg, N.; Attié, J.L. Aerosol data assimilation in the MOCAGE chemical transport model during the TRAQA/ChArMEx campaign: lidar observations. *Atmos. Meas. Tech.* **2020**, *13*, 4645–4667. https://doi.org/10.5194/amt-13-4645-2020.
36. Holben, B.; Eck, T.; Slutsker, I.; Tanre, D.; Buis, J.; Setzer, A.; Vermote, E.; Reagan, J.; Kaufman, Y.; Nakajima, T.; et al. AERONET—A federated instrument network and data archive for aerosol characterization. *Remote sensing of environment* **1998**, *66*, 1–16.
37. Royer, P.; Raut, J.C.; Ajello, G.; Berthier, S.; Chazette, P. Synergy between CALIOP and MODIS instruments for aerosol monitoring: application to the Po Valley. *Atmospheric Measurement Techniques* **2010**, *3*, 893–907. https://doi.org/10.5194/amt-3-893-2010.
38. Sasano, Y.; Browell, E.V.; Ismail, S. Error caused by using a constant extinction/backscattering ratio in the lidar solution. *Appl. Opt.* **1985**, *24*, 3929–3932. https://doi.org/10.1364/AO.24.003929.
39. Klett, J.D. Lidar inversion with variable backscatter/extinction ratios. *Appl. Opt.* **1985**, *24*, 1638–1643. https://doi.org/10.1364/AO.24.001638.
40. Kim, M.H.; Omar, A.H.; Tackett, J.L.; Vaughan, M.A.; Winker, D.M.; Trepte, C.R.; Hu, Y.; Liu, Z.; Poole, L.R.; Pitts, M.C.; et al. The CALIPSO version 4 automated aerosol classification and lidar ratio selection algorithm. *Atmospheric Measurement Techniques* **2018**, *11*, 6107–6135. https://doi.org/10.5194/amt-11-6107-2018.
41. Randriamiarisoa, H.; Chazette, P.; Couvert, P.; Sanak, J.; Mégie, G. Relative humidity impact on aerosol parameters in a Paris suburban area. *Atmospheric Chemistry and Physics* **2006**, *6*, 1389–1407. https://doi.org/10.5194/acp-6-1389-2006.
42. Cheng, Z.; Liu, D.; Yang, Y.; Yang, L.; Huang, H. Interferometric filters for spectral discrimination in high-spectral-resolution lidar: performance comparisons between Fabry–Perot interferometer and field-widened Michelson interferometer. *Appl. Opt.* **2013**, *52*, 7838–7850. https://doi.org/10.1364/AO.52.007838.
43. Eloranta, E. *High Spectral Resolution Lidar in Lidar: Range-Resolved Optical Remote Sensing of the Atmosphere*; K. Weitkamp editor, Springer-Berlag, New-York, 2005.
44. Weitkamp, C. *Lidar: Range-Resolved Optical Remote Sensing of the Atmosphere*; Springer series in optical sciences, Springer: New York, NY, 2005. https://doi.org/10.1007/b106786.
45. Orlov, D.A.; Glazenborg, R.; Ortega, R.; Kernen, E. High-detection efficiency MCP-PMTs with single photon counting capability for LIDAR applications. In Proceedings of the International Conference on Space Optics — ICSO 2018; Sodnik, Z.; Karafolas, N.; Cugny, B., Eds. International Society for Optics and Photonics, SPIE, 2019, Vol. 11180, p. 1118031. https://doi.org/10.1117/12.2536028.
46. Sič, B. Amélioration de la représentation des aérosols dans un modèle de chimie-transport: modélisation et assimilation de données. PhD thesis, Université de Toulouse, Université Toulouse III-Paul Sabatier, 2014.
47. Dong, Q.; Huang, Z.; Li, W.; Li, Z.; Song, X.; Liu, W.; Wang, T.; Bi, J.; Shi, J. Polarization Lidar Measurements of Dust Optical Properties at the Junction of the Taklimakan Desertndash;Tibetan Plateau. *Remote Sensing* **2022**, *14*. https://doi.org/10.3390/rs14030558.
48. Han, Y.; Wang, T.; Tang, J.; Wang, C.; Jian, B.; Huang, Z.; Huang, J. New insights into the Asian dust cycle derived from CALIPSO lidar measurements. *Remote Sensing of Environment* **2022**, *272*, 112906. https://doi.org/https://doi.org/10.1016/j.rse.2022.112906.
49. Xiao, D.; Wang, N.; Shen, X.; Landulfo, E.; Zhong, T.; Liu, D. Development of ZJU High-Spectral-Resolution Lidar for Aerosol and Cloud: Extinction Retrieval. *Remote Sensing* **2020**, *12*. https://doi.org/10.3390/rs12183047.
50. Chen, Q.X.; Huang, C.L.; Yuan, Y.; Tan, H.P. Influence of COVID-19 Event on Air Quality and their Association in Mainland China. *Aerosol and Air Quality Research* **2020**, *20*, 1541–1551. https://doi.org/10.4209/aaqr.2020.05.0224.
51. McPherson, C.J.; Reagan, J.A.; Schafer, J.; Giles, D.; Ferrare, R.; Hair, J.; Hostetler, C. AERONET, airborne HSRL, and CALIPSO aerosol retrievals compared and combined: A case study. *Journal of Geophysical Research: Atmospheres* **2010**, *115*. https://doi.org/https://doi.org/10.1029/2009JD012389.
52. Masutani, M.; Schlatter, T.W.; Errico, R.M.; Stoffelen, A.; Andersson, E.; Lahoz, W.; Woollen, J.S.; Emmitt, G.D.; Riishøjgaard, L.P.; Lord, S.J. Observing System Simulation Experiments. In *Data*

Assimilation; Lahoz, W.; Khattatov, B.; Menard, R., Eds.; Springer Berlin Heidelberg, 2010; pp. 647–679. https://doi.org/10.1007/978-3-540-74703-1_24.

53. Timmermans, R.; Segers, A.J.; Builtjes, P.J.; Vautard, R.; Siddans, R.; Elbern, H.; Tjemkes, S.A.; Schaap, M.; et al. The added value of a proposed satellite imager for ground level particulate matter analyses and forecasts. *IEEE J. Sel. Topics Appl. Earth Obs. Remote Sens.* **2009**, *2*, 271–283.